# Aalto University

Mölsä, Eemeli; Tiitinen, Lauri; Saarakkala, Seppo E.; Peretti, Luca; Hinkkanen, Marko

## Standstill identification of an induction motor model including deep-bar and saturation characteristics

# Standstill Identification of an Induction Motor Model Including Deep-Bar and Saturation Characteristics

Eemeli Mölsä ⬤, Lauri Tiitinen ⬤, Seppo E. Saarakkala ⬤, Luca Peretti ⬤, and Marko Hinkkanen ⬤, *Senior Member, IEEE*

*Abstract*—This article deals with standstill identification of an induction motor drive for sensorless self-commissioning purposes. The proposed identification method is based on an advanced model of a squirrel-cage induction motor. The model includes the deep-bar effect and the magnetic saturation characteristics. The excitation signals are fed to the stator using a standard inverter without compensating for its nonlinearities. The saturable stator inductance is first identified by means of a robust flux-integration test, where unknown voltage disturbances are canceled with suitably selected current pulses. Then, the deep-bar characteristics are identified by means of a dc-biased sinusoidal excitation using different frequencies. Finally, the cross-saturation characteristics of the rotor leakage inductance are identified by altering the dc bias of the excitation signal. The identified characteristics are transformed to the parameters of the advanced motor model taking into account the interrelations of the aforementioned phenomena. Since the physical phenomena affecting the standstill identification process are properly included in the identified model, fewer approximations are needed and more accurate parameter estimates are obtained. The identification procedure is validated by means of experiments using two different induction motors (5.6 and 45 kW).

*Index Terms*—Deep-bar effect, induction motor drives, parameter identification, saturation characteristics, self-commissioning.

## I. INTRODUCTION

**A** THREE-PHASE induction motor drive equipped with vector control or direct torque control is a typical solution in industrial applications. To enable its self-commissioning, the parameters (or the nonlinear characteristics) of the underlying motor model have to be identified, preferably at standstill [1], [2]. The parameters of a squirrel-cage induction motor can
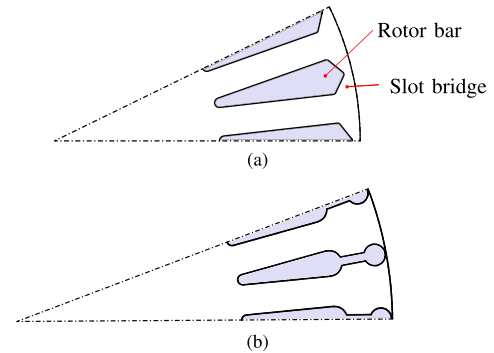
Fig. 1. Rotor cross sections. (a) 5.6-kW motor. (b) 45-kW motor. The rotor slots are closed with thin bridges. In (b), the rotor is of a double-cage type.

be divided into stator-side parameters (consisting of the stator resistance and the stator inductance) and rotor-side parameters (including the rotor leakage inductance and the rotor resistance). The stator inductance saturates as a function of the magnetizing current [3]. The rotor leakage inductance saturates highly as a function of the rotor current, if the rotor slots are closed (cf. Fig. 1) [4], [5]. Moreover, the rotor resistance depends on the rotor frequency due to the deep-bar effect [5]–[8]. All these phenomena are included in a recent advanced motor model [9]. It is to be noted that the majority of low-power induction motors are equipped with the closed rotor slots due to the manufacturing and durability reasons [10], [11].

A standard method to identify the saturable stator inductance is the no-load test [12], but it requires rotating the motor shaft. The rotor-side parameters can be identified by means of the locked-rotor test [12], which, however, is not practical for automatic self-commissioning purposes due to required mechanical arrangements. Furthermore, the standard locked-rotor test yields an overestimated value for the rotor resistance due to the deep-bar effect (if the test is carried out at the rated supply frequency) and omits the slot-bridge saturation characteristics. An advanced locked-rotor test in [9] takes these phenomena into account, but it is not suitable for automatic self-commissioning.

At standstill, the saturable stator inductance can be characterized by means of a flux-integration test, where current pulses are fed to the stator and the induced stator voltages are integrated [13]–[16]. This approach is sensitive to the stator resistance estimate and the inverter nonlinearities (the dead-time effect and the power device voltage drops) [17]. A robust version of the flux-integration test is introduced in [18],

where the unknown voltage drops are canceled using suitably selected current pulses. Hence, neither the stator resistance estimate nor the compensation for the inverter nonlinearities is needed.

In order to identify the rotor-side characteristics at standstill without locking the rotor, the excitation voltage should include angular frequencies above the inverse of the rotor time constant (since otherwise the resulting current response goes predominantly through the magnetizing branch). At such excitation frequencies already, the deep-bar effect may significantly affect the stator current response. Using the single-axis sinusoidal excitation [13], [19]–[24], the rotor-side parameters can be identified based on the stator voltage and current phasors. The excitation voltage should be sufficiently low to avoid distorted current response due to the magnetic saturation, further resulting inaccuracy of the phasors. However, low voltages are difficult to produce due to the inverter nonlinearities.

The effect of the inverter nonlinearities can be mitigated by using dc-biased sinusoidal excitation [13], [22], [24]. When interpreting the identification results, it is important to notice that the dc component of the stator current magnetizes the main-flux path, making the stator inductance dependent on the dc-bias level. In [13] and [24], this effect is mistakenly assumed to originate from the leakage inductance that saturates as a function of the stator current. The methods in [19] and [21]–[23] do not consider the magnetic saturation. None of these methods compensates for the deep-bar effect, even though its effect is mitigated by choosing a low excitation frequency. Furthermore, the cross-saturation effect between the main flux and the rotor leakage flux typically appears [25], which may distort standstill identification results if the dc bias is used.

This article is an extended version of our conference paper [26]. Based on the advanced induction motor model [9], we propose a comprehensive standstill identification procedure for an induction motor drive. The standard inverter is used to supply the excitation signals. Only the phase currents and the dc-link voltage are measured, and the compensation for the inverter nonlinearities is not needed. First, as preliminaries, the stator resistance is measured using dc injection, and the nonlinear stator inductance is identified using the robust flux-integration test [18]. These measurements are mandatory before the proposed next steps. Then, the rotor-cage impedance (i.e., the deep-bar characteristics) is identified using the dc-biased sinusoidal excitation whose frequency is varied. Finally, the cross-saturation characteristics of the rotor slot bridges are identified by altering the dc bias of the excitation signal.

Once these three characteristics have been identified, they are transferred to the parameters of the advanced induction motor model taking into account the interrelations of the aforementioned phenomena. The effect of the main-flux saturation on the rotor-side characteristics is compensated for based on the linearized motor model. If needed, the parameters of the advanced model can be readily reduced to the parameters of the conventional models. The proposed identification procedure is experimentally validated using 5.6- and 45-kW induction motors.
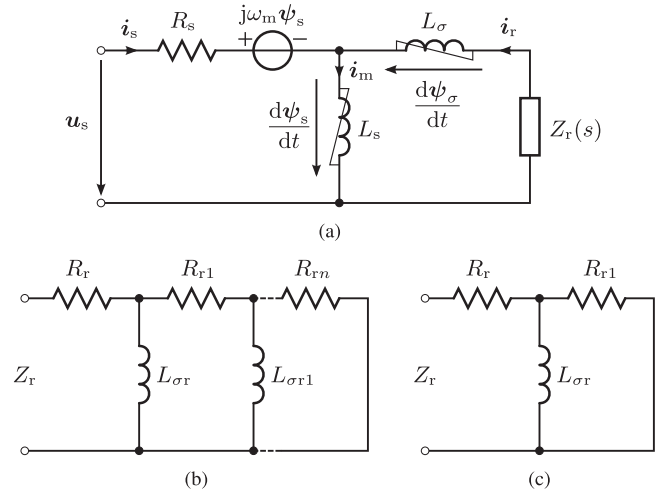


Fig. 2. Motor model in rotor coordinates. (a) Γ model including nonlinear stator inductance $L_s$, nonlinear leakage inductance $L_\sigma$, and rotor-cage impedance $Z_r$. (b) $n$th-order rotor-cage impedance. (c) First-order rotor-cage impedance, applied in the proposed method. The nonlinearity of $L_\sigma$ originates mainly from the rotor slot-bridge saturation.

## II. MOTOR MODEL

### A. Voltage and Flux Linkage Equations

Throughout this article, the space vectors and other complex quantities are marked in bold. Fig. 2(a) shows an equivalent circuit[1] for the advanced Γ model of an induction motor, including the deep-bar and saturation characteristics [9]. The model is presented in coordinates rotating at the electrical angular speed $\omega_m$ of the rotor, since the rotor-cage impedance is easiest to express in these coordinates. If needed, the model can be easily transformed to other coordinate systems. The voltage equations are

$$\frac{d\boldsymbol{\psi}_s}{dt} = \boldsymbol{u}_s - R_s \boldsymbol{i}_s - \mathrm{j}\omega_m \boldsymbol{\psi}_s \tag{1}$$

$$\frac{d\boldsymbol{\psi}_\sigma}{dt} = -\boldsymbol{u}_s + R_s \boldsymbol{i}_s + \mathrm{j}\omega_m \boldsymbol{\psi}_s - Z_r(s)\boldsymbol{i}_r \tag{2}$$

where $\boldsymbol{u}_s$ is the stator voltage, $\boldsymbol{i}_s$ is the stator current, $\boldsymbol{i}_r$ is the rotor current, $R_s$ is the stator resistance, $Z_r(s)$ is the rotor-cage impedance, and $s = d/dt$ is the differential operator.

The stator flux linkage and the rotor leakage flux linkage, respectively, are

$$\boldsymbol{\psi}_s = L_s(\boldsymbol{i}_s + \boldsymbol{i}_r) \tag{3}$$

$$\boldsymbol{\psi}_\sigma = L_\sigma \boldsymbol{i}_r \tag{4}$$

where $L_s$ is the saturable stator inductance and $L_\sigma$ is the saturable leakage inductance. The inductance $L_\sigma$ models the leakage flux at the rotor slot bridges, while the rotor-cage impedance $Z_r(s)$ takes the leakage flux through the rotor bars into account. The effect of the stator leakage flux is included in $L_s$ and $L_\sigma$ [3]. The sum of the stator and rotor currents, $\boldsymbol{i}_m = \boldsymbol{i}_s + \boldsymbol{i}_r$, is referred to as the magnetizing current.

---

[1]In equivalent circuits, there are two opposite conventions for choosing the direction of the arrow that shows the voltage drop. We use the convention, where the arrow points from the positive to the negative terminal.

## B. Saturation Characteristics

The main-flux path saturates predominantly as a function of the stator flux linkage (or, equivalently, the magnetizing current). Typically, the stator leakage-flux path does not saturate significantly. If the rotor slots are closed, the slot bridges saturate as a function of the rotor leakage flux (or the rotor current).

Induction motors also show cross-saturation effects due to skewed and closed rotor slots [25]. To include these effects, the saturable inductances can be modeled in a general form[2]

$$L_{\mathrm{s}} = L_{\mathrm{s}}(\psi_{\mathrm{s}}, \psi_{\sigma}) \qquad L_{\sigma} = L_{\sigma}(\psi_{\mathrm{s}}, \psi_{\sigma}) \qquad (5)$$

where $\psi_{\mathrm{s}} = |\boldsymbol{\psi}_{\mathrm{s}}|$ and $\psi_{\sigma} = |\boldsymbol{\psi}_{\sigma}|$ are the flux-linkage magnitudes. These functions can be represented using lookup tables or explicit functions [9], [15], [25]. If the cross saturation is omitted, the inductances $L_{\mathrm{s}} = L_{\mathrm{s}}(\psi_{\mathrm{s}})$ and $L_{\sigma} = L_{\sigma}(\psi_{\sigma})$ can be experimentally characterized by performing the no-load and locked-rotor tests, respectively [9]. The full characterization of the cross-saturation effects requires load tests [25]. If dc-bias current is used in standstill identification of the rotor-side parameters, the cross saturation may affect the results.

## C. Deep-Bar Effect

Due to the eddy currents in rotor bars, the effective rotor resistance increases and the effective rotor bar inductance decreases as a function of the rotor current frequency [4]. The rotor current frequency equals the slip frequency during normal operation, but the identification of the rotor-side parameters requires injecting higher frequencies to the rotor.

The rotor-cage impedance can be modeled using a ladder circuit shown in Fig. 2(b) [9]. To keep the transfer function $Z_{\mathrm{r}}(s)$ proper, the circuit must be terminated with a resistor according to the figure. This model can be parameterized by means of analytical expressions or performing a series of locked-rotor tests at different stator frequencies [9].

Since frequencies of only a few tens of hertz are needed in standstill identification, the first-order ladder circuit shown in Fig. 2(c) suffices for the purposes of this article. Its transfer function is

$$Z_{\mathrm{r}}(s) = R_{\mathrm{r}} + \frac{sL_{\sigma\mathrm{r}}R_{\mathrm{r}1}}{sL_{\sigma\mathrm{r}} + R_{\mathrm{r}1}}. \qquad (6)$$

As the frequency approaches zero, the resistive part of the impedance approaches $R_{\mathrm{r}}$ and the reactive part approaches $sL_{\sigma\mathrm{r}}$. Therefore, the dc rotor resistance $R_{\mathrm{r}}$ and the dc rotor-bar inductance $L_{\sigma\mathrm{r}}$ in (6) can be directly linked to the standard $\Gamma$ model: its rotor resistance corresponds to $R_{\mathrm{r}}$ and its leakage inductance corresponds to the sum $L_{\sigma} + L_{\sigma\mathrm{r}}$.

It is worth noticing that the rotor-cage impedance is described by a real-coefficient transfer function $Z_{\mathrm{r}}(s)$ since the coordinate system rotates at the rotor speed $\omega_{\mathrm{m}}$. In any other coordinate system, the equivalent transfer function has speed-dependent complex coefficients. If needed, the transfer function (6)

[2]Alternatively, the saturation characteristics can be represented in the reciprocal form $L_{\mathrm{s}} = L_{\mathrm{s}}(i_{\mathrm{m}}, i_{\mathrm{r}})$ and $L_{\sigma} = L_{\sigma}(i_{\mathrm{m}}, i_{\mathrm{r}})$. We use both forms interchangeably in this article.
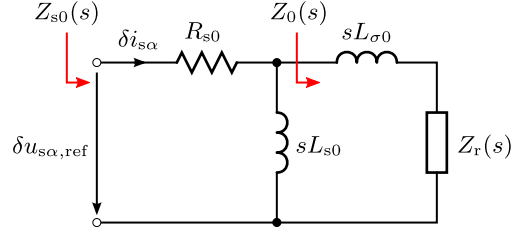


Fig. 3. Small-signal model at standstill, excited to $\alpha$-axis. The linearized model includes the operating-point stator inductance $L_{\mathrm{s}0}$, the operating-point slot-bridge inductance $L_{\sigma0}$, and the rotor-cage impedance $Z_{\mathrm{r}}(s)$.

could be written in stator coordinates via the transformation $s \mapsto s - \mathrm{j}\omega_{\mathrm{m}}$.

## III. LINEARIZED MODEL

For standstill identification, the inverter and motor models are linearized, resulting in the small-signal model shown in Fig. 3. The linearized model is based on the nonlinear model in Fig. 2(a) and includes also the operating-point voltage drop of the inverter. The motor is assumed to be at standstill, $\omega_{\mathrm{m}} = 0$. The components of the space vector are marked with the subscripts $\alpha$ and $\beta$, e.g., $\boldsymbol{u}_{\mathrm{s}} = u_{\mathrm{s}\alpha} + \mathrm{j}u_{\mathrm{s}\beta}$. Furthermore, the small-signal deviation of about the operating point is denoted by $\delta u_{\mathrm{s}\alpha} = u_{\mathrm{s}\alpha} - u_{\mathrm{s}\alpha0}$, where the subscript 0 refers to the operating point. To streamline the notation, the operating-point quantities will be marked as $u_{\mathrm{s}0} = u_{\mathrm{s}\alpha0}$ in the following equations.

### A. Inverter

The output voltage of the inverter depends nonlinearly on the current

$$u_{\mathrm{s}\alpha} = u_{\mathrm{s}\alpha,\mathrm{ref}} - u_{\mathrm{err}}(i_{\mathrm{s}\alpha}) \qquad (7)$$

where $u_{\mathrm{s}\alpha,\mathrm{ref}}$ is the voltage reference and $u_{\mathrm{err}}$ represents the voltage-error characteristics caused by the inverter nonlinearities. Fig. 4(a) shows typical voltage-error characteristics. Linearizing (7) about the operating point yields

$$\delta u_{\mathrm{s}\alpha} = \delta u_{\mathrm{s}\alpha,\mathrm{ref}} - R_{\mathrm{i}0}\delta i_{\mathrm{s}\alpha} \qquad (8)$$

where $R_{\mathrm{i}0} = (\partial u_{\mathrm{err}}/\partial i_{\mathrm{s}\alpha})_0$ is the incremental inverter resistance. Therefore, the incremental stator resistance seen by the control system is $R_{\mathrm{s}0} = R_{\mathrm{s}} + R_{\mathrm{i}0}$, if the inverter voltage error is not compensated for.

### B. Motor at Standstill

The dc-bias voltage $u_{\mathrm{s}\alpha0} = u_{\mathrm{s}0}$ and the small-signal excitation voltage $\delta u_{\mathrm{s}\alpha}$ are fed to the $\alpha$-axis direction while $u_{\mathrm{s}\beta0} = 0$ and $\delta u_{\mathrm{s}\beta} = 0$. The operating point is defined by the dc bias $u_{\mathrm{s}0} = R_{\mathrm{s}0}i_{\mathrm{s}0}$. The operating-point rotor current is $i_{\mathrm{r}0} = 0$, and correspondingly, $\psi_{\sigma0} = 0$. Consequently, the operating-point stator flux is $\psi_{\mathrm{s}0} = L_{\mathrm{s}}(\psi_{\mathrm{s}0}, 0)i_{\mathrm{s}0}$. The linearization of the model leads to the operating-point incremental inductances

$$L_{\mathrm{s}0} = \left(\frac{\partial\psi_{\mathrm{s}}}{\partial i_{\mathrm{m}}}\right)_0, \qquad L_{\sigma0} = \left(\frac{\partial\psi_{\sigma\mathrm{b}}}{\partial i_{\mathrm{r}}}\right)_0. \qquad (9)$$
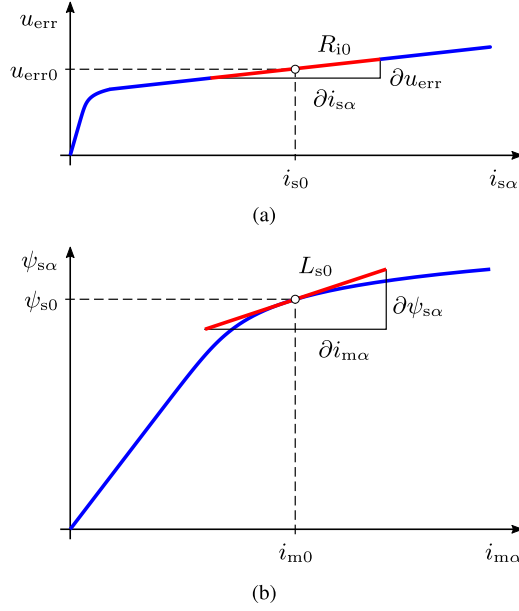
Fig. 4. Nonlinear characteristics. (a) Inverter voltage error. (b) Stator flux linkage. The definitions of the incremental inverter resistance $R_{i0}$ and the incremental inductance $L_{s0}$ are illustrated in (a) and (b), respectively. The inverter nonlinearity originates from the dead-time effect and the voltage drop of power devices. The resistance $R_{i0}$ is essentially constant, except at the lowest currents.
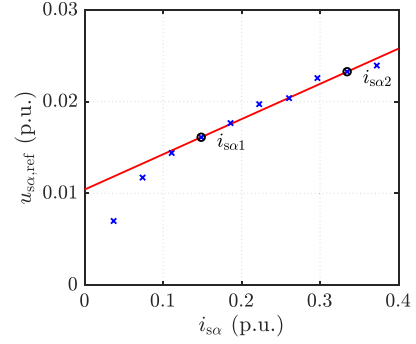


Fig. 5. Measured voltage reference characteristics as the dc currents are fed to the 5.6-kW motor. The red line represents the slope corresponding to $R_{s0} = R_s + R_{i0}$, estimated using two operating points (black markers).
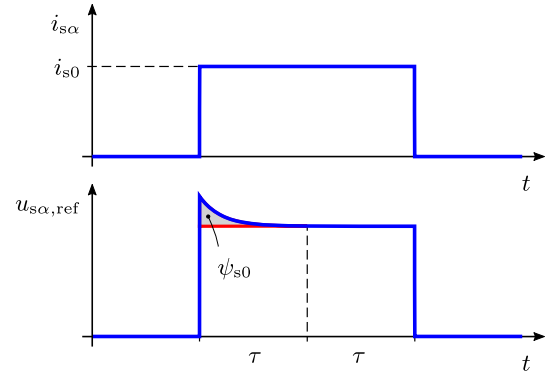


Fig. 6. Principle of the robust flux-integration test. The first integration period of $\tau$ includes the voltage induced from the flux linkage. The second integration period includes only the voltage drop due to the stator resistance and the inverter.

In the single-axis test at standstill, both incremental inductances depend only on $\psi_{s0}$ (or $i_{m0} = i_{s0}$) while $i_{r0} = 0$, as explained above. Fig. 4(b) shows an example of the stator-flux saturation characteristics and the incremental stator inductance at an operating point. Due to the symmetries of any feasible saturation characteristics about $i_{r0} = 0$, the cross saturation does not result in additional incremental inductances in the linearized model. However, the incremental leakage inductance $L_{\sigma 0} = L_{\sigma 0}(\psi_{s0}, 0)$ depends on $\psi_{s0}$ due to the cross saturation. In the Laplace domain, the stator impedance of the small-signal model in Fig. 3 is

$$Z_{s0}(s) = \frac{\delta u_{s\alpha,\text{ref}}(s)}{\delta i_{s\alpha}(s)} = R_{s0} + \frac{sL_{s0}Z_0(s)}{sL_{s0} + Z_0(s)} \quad (10)$$

where the impedance of the rotor branch

$$Z_0(s) = sL_{\sigma 0} + Z_r(s) \quad (11)$$

consists of the leakage impedance $sL_{\sigma 0}$ and the rotor-cage impedance $Z_r(s)$.

## IV. IDENTIFICATION METHOD

### A. Stator Resistance

The effective stator resistance $R_{s0}$ seen by the control system can be estimated by means of two (or more) dc operating points. Due to the inverter nonlinearities, the slope of the current is nonlinear at low voltages, but becomes almost linear when the voltage increases. The operating-point resistance can be estimated as

$$R_{s0} = \frac{u_{s\alpha,\text{ref}2} - u_{s\alpha,\text{ref}1}}{i_{s\alpha 2} - i_{s\alpha 1}} \quad (12)$$

where $i_{s\alpha 1}$ and $i_{s\alpha 2}$ are the dc currents in the linear operating region of the inverter and $u_{s\alpha,\text{ref}1}$ and $u_{s\alpha,\text{ref}2}$ are the corresponding voltage references. Fig. 5 shows an example of the measured inverter output voltage characteristics. Using more than two operating points would allow us to reduce the effect of noise and other disturbances.

### B. Stator Inductance

The robust flux-integration test [18] is applied to identify the saturable stator inductance. DC current steps are supplied to the stator using a current controller.[3] Fig. 6 shows the stator voltage reference $u_{s\alpha,\text{ref}}$ that decays to its steady-state value during the regulated current step. The stator flux linkage is estimated as

$$\psi_{s0}(i_{s0}) = \int_0^\tau u_{s\alpha,\text{ref}}dt - \int_\tau^{2\tau} u_{s\alpha,\text{ref}}dt \quad (13)$$

where $i_{s0}$ is the amplitude of the regulated dc current and $u_{s\alpha,\text{ref}}$ is the stator voltage reference. The integration time $\tau$ has to be sufficiently long time to ensure that the stator flux has been converged to its steady-state value, which generally takes approximately five rotor time constants. A simple choice is to

---

[3]Since the motor model parameters are not known in advance, the current controller can be tuned using rough parameter estimates. The bandwidth should be low in order to ensure stability.
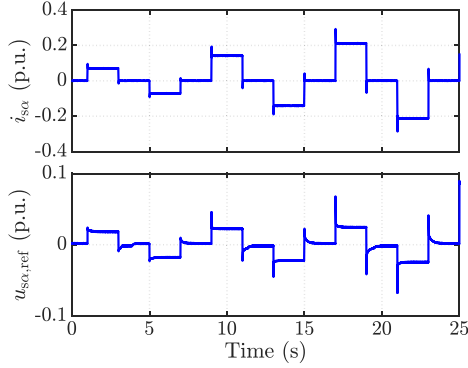
Fig. 7. Measured flux-integration test sequence for the 5.6-kW motor.

define the integration time $\tau = 5\tau_r$, where $\tau_r$ is a rough estimate for the rotor time constant [18].

During the first time period, from 0 to $\tau$, the stator voltage reference $u_{s\alpha,\mathrm{ref}}$ includes the induced voltage. At time instant $\tau$, the stator voltage (and stator flux) is assumed to have converged to its steady-state value and to consist only of the voltage drop due to the stator resistance and the inverter. Thus, during the second time period, from $\tau$ to $2\tau$, the stator voltage includes the voltage drop of the stator resistance and the inverter but not the induced voltage. As both time periods include the same voltage drop, the resistive term is ruled out without explicitly determining it. Thus, the voltage reference sent to the pulsewidth modulator $u_{s\alpha,\mathrm{ref}}$ can be directly used in (13).

In order to capture the saturation characteristics of the stator inductance, the test is repeated at different current magnitudes. Fig. 7 shows an example of the measured test sequence. The effect of the possible offset at the phase current measurement is mitigated by repeating the test with both positive and negative currents and by computing the average of the obtained two flux linkage estimates.

For each dc current value, the chord-slope stator inductance is given by $L_s = \psi_{s0}/i_{s0}$, where $\psi_{s0}$ is obtained from (13). The identified inductance values can be stored in a lookup table. Alternatively, an explicit function can be fitted to the identified inductance values. In this article, an explicit function is used

$$L_s(\psi_s) = \frac{L_{su}}{1 + (\psi_s/c)^S} \tag{14}$$

where $L_{su}$ is the unsaturated inductance, and $c$ and $S$ are positive constants [15]. The corresponding operating-point incremental inductance is

$$L_{s0}(\psi_s) = \frac{L_{su}}{1 + (1 + S)(\psi_s/c)^S} \tag{15}$$

which is needed in identification of the rotor-side parameters.

### C. Rotor-Cage Impedance

The three parameters of the rotor-cage impedance model (6) are identified. The excitation signal is

$$u_{s\alpha,\mathrm{ref}}(t) = u_{s0} + u_1 \sin(\omega t) \tag{16}$$

where $u_{s0}$ is the dc-bias voltage and $u_1$ is the amplitude of the signal. The excitation frequency $\omega$ must be adequately high, since the frequencies lower than the inverse rotor time constant access primarily the main-flux path. The dc bias is used to maintain the current in the linear operating region of the inverter [cf. Fig. 4(a)], in order to decrease the effect of the nonlinearities. The amplitude $u_1$ should be adequately low to stay in the small-signal range to permit the use of the model (10).

The stator impedance is calculated from the measurements as

$$\boldsymbol{Z}_{s0}(\mathrm{j}\omega) = \frac{\delta \boldsymbol{u}_{s\alpha,\mathrm{ref}}(\omega)}{\delta \boldsymbol{i}_{s\alpha}(\omega)} \tag{17}$$

where $\delta \boldsymbol{u}_{s\alpha,\mathrm{ref}}$ and $\delta \boldsymbol{i}_{s\alpha}$ are the complex phasors obtained from the phase voltage references and the measured phase currents, respectively. The phasors can be computed, e.g., using the discrete Fourier transform (DFT) or the sliding DFT [27]. The impedance of the rotor branch solved from (10) and (11) is

$$\boldsymbol{Z}_0(\mathrm{j}\omega) = \frac{\mathrm{j}\omega L_{s0}[\boldsymbol{Z}_{s0}(\mathrm{j}\omega) - R_{s0}]}{\mathrm{j}\omega L_{s0} + R_{s0} - \boldsymbol{Z}_{s0}(\mathrm{j}\omega)}. \tag{18}$$

Therefore, as the stator impedance $\boldsymbol{Z}_{s0}(\mathrm{j}\omega)$ is known after the measurement, and the incremental stator inductance $L_{s0}$ in the operating point is known after the robust flux-integration test, the rotor-branch impedance can be calculated from (18) for each $\omega$ and $i_{s0}$. The incremental inductance $L_{s0} = L_{s0}(\psi_{s0})$ needed in (18) can be computed using (15) for each bias flux $\psi_{s0} = L_s(\psi_{s0})i_{s0}$. It is worth noticing that the dc-bias current may saturate the stator inductance, but this effect is taken into account in (18) using the results from the flux-integration method, as explained above.

According to (11), the resistive rotor-cage impedance equals the resistive rotor-branch impedance

$$\mathrm{Re}\{\boldsymbol{Z}_r(\mathrm{j}\omega)\} = \mathrm{Re}\{\boldsymbol{Z}_0(\mathrm{j}\omega)\} \tag{19}$$

and does not depend on $L_{\sigma 0}$. Therefore, the parameters $L_{\sigma r}$, $R_r$, and $R_{r1}$ of the rotor-cage impedance model (6) can be estimated by means of fitting the resistive part $\mathrm{Re}\{\boldsymbol{Z}_r(\mathrm{j}\omega)\}$ of the model to the measured values $\mathrm{Re}\{\boldsymbol{Z}_0(\mathrm{j}\omega)\}$. A minimum of three different excitation frequencies are needed to estimate the three parameters.

The dc rotor resistance $R_r$ and the dc inductance $L_{\sigma r}$ can be directly used to parameterize the standard $\Gamma$ model for control purposes (while the parameter $R_{r1}$ is not needed). Alternatively, if high accuracy at large slip frequencies is needed, the first-order ladder circuit with all three parameters can be used in control.

### D. Leakage Inductance

In the frequency domain, the incremental leakage inductance $L_{\sigma 0}$ can be solved from the imaginary part of (11) as

$$L_{\sigma 0} = \frac{\mathrm{Im}\{\boldsymbol{Z}_0(\mathrm{j}\omega) - \boldsymbol{Z}_r(\mathrm{j}\omega)\}}{\omega}. \tag{20}$$

The incremental leakage inductance can be estimated using the impedance of the rotor branch (18), based on the measured stator impedance (17), and the parameterized rotor-cage impedance model (6). If the stator impedance in (17) is measured at different
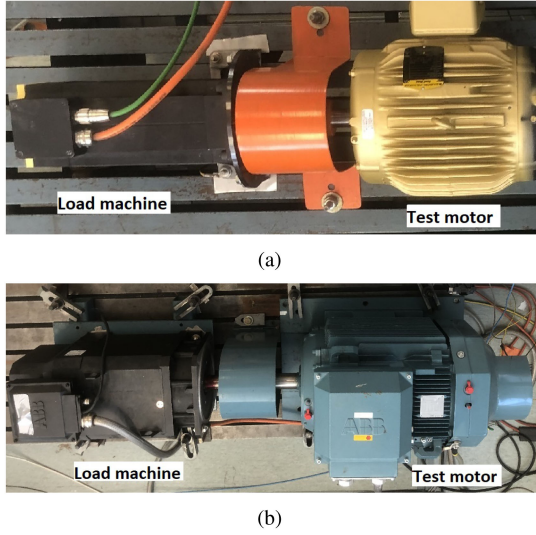
Fig. 8. Experimental setups. (a) 5.6-kW motor. (b) 45-kW motor. The load machines are not actively used in this article.

dc-bias currents, the effect of the cross saturation on $L_{\sigma 0}$ can be captured.

## V. EXPERIMENTAL RESULTS

### A. Experimental System

The proposed identification method is validated by means of experiments using commercial 5.6- and 45-kW induction motors. Fig. 1 shows the rotor cross sections of these motors. Both motors have closed rotor slots. The 5.6-kW motor has triangular-shaped rotor bars and the 45-kW motor has a double-cage rotor.

A three-phase inverter, controlled by a dSPACE MicroLab-Box system, is used to supply the motor under tests. The experimental setups are shown in Fig. 8. The stator currents and the dc-link voltage are measured at the sampling frequency of 4 kHz. The switching frequency is 2 kHz. The duty ratio references are calculated from the voltage reference, using the measured dc-link voltage. The effect of the computational and pulsewidth modulation delays on the realized voltage is compensated for, while the inverter nonlinearities are left uncompensated.

### B. Benchmark Results

The benchmark characteristics of the motors were measured using sinusoidal voltage supply and a calibrated data logger, according to the procedure described in [9]. A series of no-load tests was performed using different stator flux (or magnetizing current) levels in order to obtain the saturable stator inductance. The rotor-cage impedance was measured by completing a series of locked-rotor tests at different stator frequencies. Moreover, the leakage inductance was measured by conducting another series of locked-rotor tests, while keeping the stator frequency constant and varying the stator current amplitude instead. Fig. 9 shows the results of the no-load tests for both motors. Figs. 10
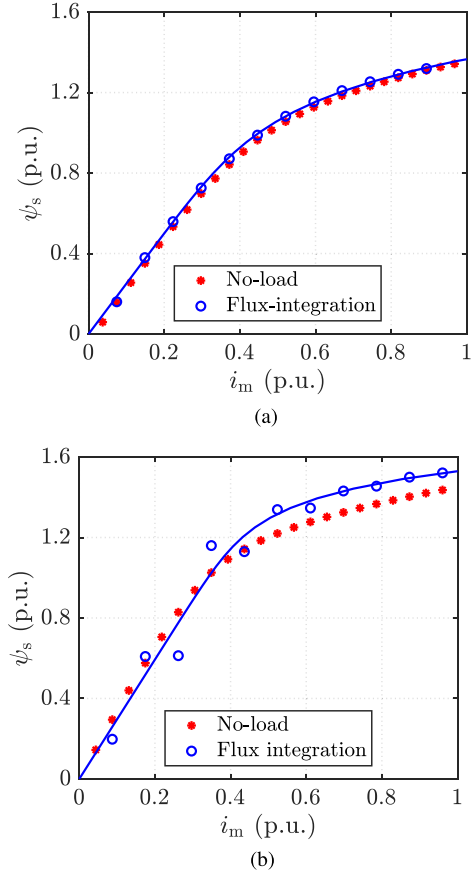


Fig. 9. Stator flux linkage as a function of the magnetizing current. (a) 5.6-kW motor. (b) 45-kW motor. The red markers are the benchmark values obtained from the no-load tests. The blue markers are the results from the robust flux-integration tests. The solid line corresponds to the model (14) fitted to the flux-integration test.

and 11 show the measured rotor-cage impedance and the leakage inductance, respectively.

### C. Proposed Standstill Identification

*1) Stator Resistance:* The effective stator resistance $R_{s0}$ is estimated by injecting two dc currents to the stator and using (12). The current magnitudes were $i_{s\alpha 1} = 0.15$ p.u. and $i_{s\alpha 2} = 0.35$ p.u. The estimated values are given in Table I.

*2) Stator Inductance:* The nonlinear stator inductance is estimated using the robust flux-integration test, as described in Section IV-B. Fig. 9 shows the identified stator flux linkage values together with the fitted saturation model (14). In the case of the 5.6-kW motor, the estimated data points and the fitted model are close to the benchmark no-load test results as shown in Fig. 9(a). In the case of the 45-kW motor, the estimated data points differ from the benchmark data points. This difference probably originates from magnetic remanence of the motor. However, the fitted model is relatively close to the benchmark characteristics. The parameters of the fitted saturation model are given in Table I.

*3) Rotor-Cage Impedance:* The rotor-cage impedance is identified using the test described in Section IV-C. In order to

TABLE I
PARAMETERS OF THE FOUR-POLE INDUCTION MOTORS

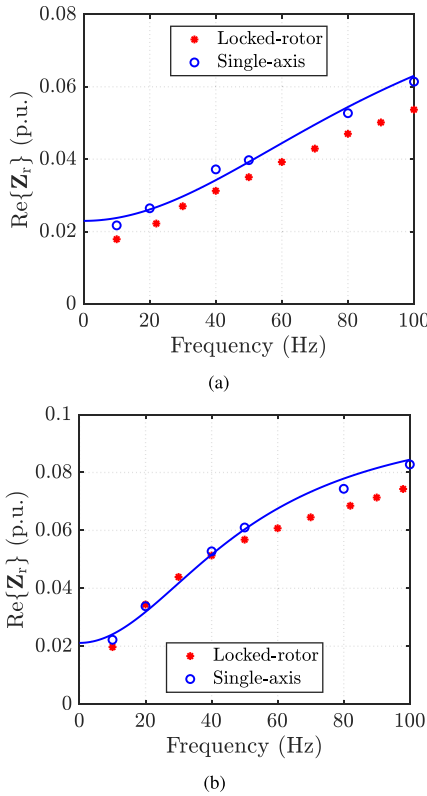| | 5.6-kW motor | 45-kW motor |
|---|---|---|
| Rated values | | |
| Voltage (line-neutral, peak value) | $\sqrt{2/3}\cdot460$ V (1 p.u.) | $\sqrt{2/3}\cdot400$ V (1 p.u.) |
| Current (peak value) | $\sqrt{2}\cdot9.5$ A (1 p.u.) | $\sqrt{2}\cdot81$ A (1 p.u.) |
| Frequency | 60 Hz (1 p.u.) | 50 Hz (1 p.u.) |
| Speed | 1770 r/min (0.983 p.u.) | 1477 r/min (0.985 p.u.) |
| Stator resistance $R_{s0}$ | 0.93 $\Omega$ (0.033 p.u.) | 61 m$\Omega$ (0.021 p.u.) |
| Stator inductance | | |
| Unsaturated inductance $L_{su}$ | 185.7 mH (2.50 p.u.) | 27.1 mH (2.99 p.u.) |
| Coefficient $c$ | 1.40 Vs (1.41 p.u.) | 1.60 Vs (1.54 p.u.) |
| Coefficient $S$ | 6 | 10 |
| Incremental leakage inductance $L_{\sigma0}$ (at $i_{s0} = 0.5$ p.u.) | 12.4 mH (0.17 p.u.) | 2.0 mH (0.22 p.u.) |
| Rotor-cage impedance | | |
| DC-inductance $L_{\sigma r}$ | 3.6 mH (0.048 p.u.) | 0.71 mH (0.078 p.u.) |
| DC-resistance $R_r$ | 0.64 $\Omega$ (0.023 p.u.) | 60.3 m$\Omega$ (0.021 p.u.) |
| Resistance $R_{r1}$ | 2.1 $\Omega$ (0.078 p.u.) | 230 m$\Omega$ (0.079 p.u.) |



Fig. 10. Resistive part of the rotor-branch impedance. (a) 5.6-kW motor. (b) 45-kW motor. The red markers are the benchmark values, obtained from the locked-rotor tests with the stator current magnitude $i_{s0} = 0.33$ p.u. The solid lines correspond to the model (6) fitted to the proposed single-axis test (blue markers). The dc-bias currents are $i_{s0} = 0.40$ p.u. (5.6-kW motor) and $i_{s0} = 0.35$ p.u. (45-kW motor).
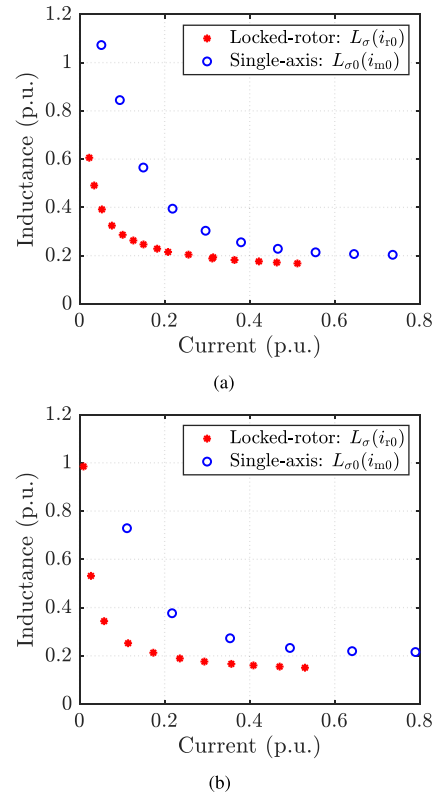


Fig. 11. Identified leakage inductance. (a) 5.6-kW motor. (b) 45-kW motor. The red markers are the values obtained from the locked-rotor tests. The blue markers are the identified values (20), obtained from the proposed single-axis test.

keep the current amplitude approximately constant, the amplitude of the excitation voltage is chosen as $u_1 = k\omega$, where the constant $k = 0.008$ p.u.

Fig. 10 shows the resistive part of the rotor-branch impedance (18) calculated from the measured stator impedance. The solid curve represents the ladder circuit model (6) fitted to the

impedance values. It can be seen that the model fits very well to the data. The dc offset values in the impedance calculated using (18) depend on the stator resistance estimate. The benchmark results from the locked-rotor test show similar dependence on the stator resistance estimate.

Since the current and dc-bus voltage measurement channels of the inverter were not calibrated, some dc offset difference between the proposed and benchmark test results could be

expected, as also visible in Fig. 10. However, perfectly accurate parameters are not needed for control purposes, but parameters should match with imperfectly calibrated measurement channels of the inverter instead. Table I gives the fitted parameters of the cage-impedance model.

*4) Leakage Inductance:* Fig. 11 shows the identified incremental leakage inductance $L_{\sigma 0}$ calculated from the measured stator impedance using (20), as a function of the bias current. The results from the locked-rotor tests are also shown, corresponding to the chord-slope inductance $L_\sigma$ as a function of the rotor current. In the case of both motors, the results from the locked-rotor test show that the leakage inductance $L_\sigma$ saturates highly as a function of the rotor current $i_{r0}$. This saturation originates from the rotor slot bridges. Furthermore, the saturation characteristics $L_{\sigma 0}(i_{m0})$ measured with the single-axis test are similar to the characteristics $L_\sigma(i_{r0})$, especially at high currents, as can be seen in Fig. 11. This result indicates a strong cross-saturation effect.

It is worth noticing that the results of the locked-rotor test and the results of the proposed single-axis test are functions of the two different currents (since it is not possible to feed dc currents to the rotor at standstill without locking the rotor). However, these identified incremental inductance values can be used to approximate the total leakage inductance for motor control purposes. The identified incremental inductance values at the nominal magnetizing current are given in Table I. For control purposes, the total leakage inductance of the standard $\Gamma$ model may be approximated as a sum $L_{\sigma 0} + L_{\sigma r}$.

## VI. CONCLUSION

The article proposes a comprehensive procedure to identify the induction motor model at standstill, using a standard inverter without compensation for the inverter nonlinearities. The proposed method is based on the advanced motor model equipped with deep-bar and saturation characteristics, which enables robust transfer of the measured data to the model characteristics. The experimental results show that the identified characteristics of the proposed method correspond very well to the benchmark data. The cross-saturation characteristics of the rotor leakage inductance can be used to approximate the chord-slope value of the total leakage inductance, which is difficult to measure without locking the rotor. The proposed identification method is suitable for a large variety of induction motors. Moreover, the identified advanced motor model can be reduced to the standard $\Gamma$ model.

## REFERENCES

[1] H. A. Toliyat, E. Levi, and M. Raina, "A review of RFO induction motor parameter estimation techniques," *IEEE Trans. Energy Convers.*, vol. 18, no. 2, pp. 271–283, Jun. 2003.

[2] S. A. Odhano, P. Pescetto, H. A. A. Awan, M. Hinkkanen, G. Pellegrino, and R. Bojoi, "Parameter identification and self-commissioning in ac motor drives: A technology status review," *IEEE Trans. Power Electron.*, vol. 34, no. 4, pp. 3603–3614, Apr. 2019.

[3] G. R. Slemon, "Modelling of induction machines for electric drives," *IEEE Trans. Ind. Appl.*, vol. 25, no. 6, pp. 1126–1131, Nov./Dec. 1989.

[4] S. Williamson and M. C. Begg, "Calculation of the bar resistance and leakage reactance of cage rotors with closed slots," in *Proc. Inst. Elect. Eng. B., Electr. Power Appl.*, vol. 132, no. 3, pp. 125–132, May 1985.

[5] A. C. Smith, R. C. Healey, and S. Williamson, "A transient induction motor model including saturation and deep bar effect," *IEEE Trans. Energy Convers.*, vol. 11, no. 1, pp. 8–15, Mar. 1996.

[6] R. C. Healey, S. Williamson, and A. C. Smith, "Improved cage rotor models for vector controlled induction motors," *IEEE Trans. Ind. Appl.*, vol. 31, no. 4, pp. 812–822, Jul./Aug. 1995.

[7] S. D. Sudhoff, D. C. Aliprantis, B. T. Kuhn, and P. L. Chapman, "An induction machine model for predicting inverter-machine interaction," *IEEE Trans. Energy Convers.*, vol. 17, no. 2, pp. 203–210, Jun. 2002.

[8] S. D. Sudhoff, D. C. Aliprantis, B. T. Kuhn, and P. L. Chapman, "Experimental characterization procedure for use with an advanced induction machine model," *IEEE Trans. Energy Convers.*, vol. 18, no. 1, pp. 48–56, Mar. 2003.

[9] E. Mölsä, S. E. Saarakkala, M. Hinkkanen, A. Arkkio, and M. Routimo, "A dynamic model for saturated induction machines with closed rotor slots and deep bars," *IEEE Trans. Energy Convers.*, vol. 35, no. 1, pp. 157–165, Mar. 2020.

[10] A. Boglietti, R. I. Bojoi, A. Cavagnino, P. Guglielmi, and A. Miotto, "Analysis and modeling of rotor slot enclosure effects in high-speed induction motors," *IEEE Trans. Ind. Appl.*, vol. 48, no. 4, pp. 1279–1287, Jul./Aug. 2012.

[11] J. Pyrhönen, T. Jokinen, and V. Hrabovcová, *Design of Rotating Electrical Machines*. Chippenham, U.K.: Wiley, 2008.

[12] *Standard Test Procedure for Polyphase Induction Motors and Generators*, IEEE Standard 112–2017, 2018.

[13] L. Peretti and M. Zigliotto, "Automatic procedure for induction motor parameter estimation at standstill," *IET Electr. Power Appl.*, vol. 6, no. 4, pp. 214–224, Apr. 2012.

[14] C. Sukhapap and S. Sangwongwanich, "Auto tuning of parameters and magnetization curve of an induction motor at standstill," in *Proc. IEEE Int. Conf. Ind. Technol.*, Bangkok, Thailand, Dec. 2002, vol. 1, pp. 101–106.

[15] N. R. Klaes, "Parameter identification of an induction machine with regard to dependencies on saturation," *IEEE Trans. Ind. Appl.*, vol. 29, no. 6, pp. 1135–1140, Nov./Dec. 1993.

[16] S. Khamehchi, E. Mölsä, and M. Hinkkanen, "Comparison of standstill parameter identification methods for induction motors," in *Proc. IEEE Symp. Sensorless Control Elect. Drives*, Helsinki, Finland, Sep. 2018, pp. 156–161.

[17] J.-W. Choi and S.-K. Sul, "Inverter output voltage synthesis using novel dead time compensation," *IEEE Trans. Power Electron.*, vol. 11, no. 2, pp. 221–227, Mar. 1996.

[18] F. Erturk and B. Akin, "A robust method for induction motor magnetizing curve identification at standstill," *IEEE Access*, vol. 7, pp. 55 422–55431, 2019.

[19] R. J. Kerkman, J. D. Thunes, T. M. Rowan, and D. W. Schlegel, "A frequency-based determination of transient inductance and rotor resistance for field commissioning purposes," *IEEE Trans. Ind. Appl.*, vol. 32, no. 3, pp. 577–584, May/Jun. 1996.

[20] A. Gastli, "Identification of induction motor equivalent circuit parameters using the single-phase test," *IEEE Trans. Energy Convers.*, vol. 14, no. 1, pp. 51–56, Mar. 1999.

[21] S. Lee, A. Yoo, H. Lee, Y. Yoon, and B. Han, "Identification of induction motor parameters at standstill based on integral calculation," *IEEE Trans. Ind. Appl.*, vol. 53, no. 3, pp. 2130–2139, May/Jun. 2017.

[22] G. Shen, K. Wang, W. Yao, K. Lee, and Z. Lu, "DC biased stimulation method for induction motor parameters identification at standstill without inverter nonlinearity compensation," in *Proc. IEEE Energy Convers. Congr. Expo.*, Denver, CO, USA, Sep. 2013, pp. 5123–5130.

[23] H. Ge, J.Guo B.Bilgin J.Ye V.Loukanov, and A. Emadi, "A reduced-order model based induction machine self-commissioning method," in *Proc. IEEE Transp. Electrif. Conf. Expo.*, Dearborn, MI, USA, Jun. 2015, pp. 1–8.

[24] M. Carraro and M. Zigliotto, "Automatic parameter identification of inverter-fed induction motors at standstill," *IEEE Trans. Ind. Electron.*, vol. 61, no. 9, pp. 4605–4613, Sep. 2014.

[25] T. Tuovinen, M. Hinkkanen, and J. Luomi, "Modeling of saturation due to main and leakage flux interaction in induction machines," *IEEE Trans. Ind. Appl.*, vol. 46, no. 3, pp. 937–945, May/Jun. 2010.

[26] E. Mölsä, L. Tiitinen, S. Saarakkala, L. Peretti, and M. Hinkkanen, "Standstill self-commissioning of an induction motor drive," in *Proc. IEEE Energy Convers. Congr. Expo.*, Detroit, MI, USA, Oct. 2020, pp. 3044–3050.

[27] E. Jacobsen and R. Lyons, "The sliding DFT," *IEEE Signal Process. Mag.*, vol. 20, no. 2, pp. 74–80, Mar. 2003.

**Eemeli Mölsä** received the B.Eng. degree in electrical engineering from the Metropolia University of Applied Sciences, Helsinki, Finland, in 2012, and the M.Sc.(Tech.) degree in electrical engineering in 2015 from Aalto University, Espoo, Finland, where he is currently working toward the D.Sc.(Tech.) degree.

His research interests include the control of electric drives.

**Lauri Tiitinen** received the B.Sc.(Tech.) and M.Sc.(Tech.) degrees in electrical engineering in 2019 and 2020, respectively, from Aalto University, Espoo, Finland, where he is currently working toward the D.Sc.(Tech.) degree.

His research interests include control and self-commissioning of electric motor drives.

**Seppo E. Saarakkala** received the M.Sc.(Eng.) degree in electrical engineering from the Lappeenranta University of Technology, Lappeenranta, Finland, in 2008, and the D.Sc.(Tech.) degree in electrical engineering from Aalto University, Espoo, Finland, in 2014.

From 2010 to 2020, he was with the School of Electrical Engineering, Aalto University, where he was a Postdoctoral Research Scientist from 2015 to January 2020. Since January 2020, he has been with Sulzer Pumps Finland Oy, Helsinki, Finland, where he is currently a Product Research and Development Engineer. His main research interests include control systems and electric drives.

Dr. Saarakkala was the co-recipient of the 2018 IEEE Industry Applications Society Industrial Drives Committee Best Paper Award and the 2020 Semikron Innovation Award.

**Luca Peretti** received the M.Sc. degree in electronic engineering from the University of Udine, Udine, Italy, in 2005, and the Ph.D. degree in mechatronics and industrial system from the University of Padova, Padova, Italy, in 2009.

From November 2007 to March 2008, he was a Visiting Ph.D. Student with ABB Corporate Research, Västerås, Sweden, where he was a Principal Scientist, Project Leader, and Strategy Coordinator, from August 2010 to August 2018. Since July 2016, he has been an Affiliated Faculty Member with the Division of Electric Power and Energy Systems, KTH Royal Institute of Technology, Stockholm, Sweden, where he has also been an Associate Professor of Electric Machines and Drives since September 2018. His main research interests include automatic parameter estimation in electric machines, sensorless control, loss segregation in drive systems, multiphase drives, and condition monitoring of machines and drives, in the context of industrial, wind energy, and traction applications.

**Marko Hinkkanen** (Senior Member, IEEE) received the M.Sc.(Eng.) and D.Sc.(Tech.) degrees in electrical engineering from the Helsinki University of Technology, Espoo, Finland, in 2000 and 2004, respectively.

He is currently an Associate Professor with the School of Electrical Engineering, Aalto University, Espoo. His research interests include control systems, electric drives, and power converters.

Dr. Hinkkanen was the General Co-Chair for the 2018 IEEE 9th International Symposium on Sensorless Control for Electrical Drives. He was the co-recipient of the 2016 International Conference on Electrical Machines Brian J. Chalmers Best Paper Award, the 2016 and 2018 IEEE Industry Applications Society Industrial Drives Committee Best Paper Awards, and the 2020 Semikron Innovation Award. He is an Associate Editor for IEEE TRANSACTIONS ON ENERGY CONVERSION and *IET Electric Power Applications*.